Internal Tides Observed by an Acoustic Doppler Current Profiler

R. F. MARSDEN AND K. C. GREENWOOD

Department of Physics, Royal Roads Military College, Victoria, British Columbia, Canada

(Manuscript received 8 December 1992, in final form 28 April 1993)

ABSTRACT

Previous studies of Knight Inlet, British Columbia, revealed the presence of a strong internal M_2 tide. Most of the energy was found to be in either the first or second dynamic modes. Due to difficulties in sampling of the surface layer, objective estimates of the distribution of tidal energy and reflection coefficients, until now, have been impossible to obtain. During June and July 1989, an intense acoustic Doppler current profiler (ADCP) sampling of the inlet was conducted. These results are used to show the existence of a strong semidiurnal flow in the baroclinic field. The authors propose that the horizontal phase information inherent in the spatial sampling by the ADCP can be used to resolve the distribution of energy between dynamic modes. Through a least squares fit of the data to a simple free wave propagation model of the inlet, the authors arrive at objective estimates of the distribution of M_2 internal tide energy. The fitting procedure is found to be sensitive to fluctuations in the basin width. When an accurate estimate of width is incorporated into the fit, the authors arrive at net energy fluxes of 0.44×10^6 W toward the mouth of the inlet at Protection Point and 1.17×10^6 W toward the head of the inlet at Tomakstum Island. It is shown that these results do not display the degeneracy inherent in other estimates and that they are in agreement with a recent numerical model of the inlet by Stacey and Pond.

1. Introduction

Knight Inlet, shown in Fig. 1, is a long, deep inlet of glacial origin on the British Columbia coast. Due to its regular width, generally steep sides, and lack of subsidiary inlets over the uppermost 100 km, it has been the subject of frequent study since the late 1950s. It is connected to the sea via Queen Charlotte Strait. Two sills restrict access to the inner basin of the inlet: the first, or inner sill, is 74 km from the head and has a maximum depth of 60 m, while the second (not shown in the figure) is 110 km from the head and rises to 65 m. The inner basin has a maximum depth of 530 m, while the outer basin does not exceed 250 m. At the head, the Franklin and Klinaklini Rivers provide a large influx of freshwater, which causes the inlet to become highly stratified. During the summer, the upper layer has a salinity of less than 5 psu near the head, with a very sharply defined interface, 2–3 m thick, at about 10 m depth. At the inner sill, the surface salinity increases to about 10 psu and the interface becomes less well defined.

The major forcing mechanism for the inlet is the barotropic tide. Assuming a mean inlet depth of about 400 m, the external Rossby radius of deformation is about 3000 km, much larger than either its length (120 km) or width (3 km). Consequently, the barotropic flow is well represented by an irrotational standing wave. Greenwood et al. (1994, henceforth referred to as GMB) have shown good agreement between the directly measured barotropic component of the flow and a pure standing wave model. Of particular interest, however, is the energy transferred from the barotropic to the baroclinic tide due to the interaction of the flow with the bottom topography and stratification at the two sills. Based on an analysis of four current meter records, Freeland and Farmer (1980) concluded that 95% of the energy dissipation rate of the barotropic tide was due to a transfer of energy to the internal tide and to an internal hydraulic jump. The remainder was due to side wall and bottom friction. Stacey (1985) modified a model by Stigebrandt (1976, 1979, 1980) to estimate internal tide generation at the inner sill. Based on tide gauge and hydrographic data sampled in 1977 and 1978, he found that mode 1 generally dominated with an energy flux greater than 2.0×10^6 W propagating away from the sill. Modes 2 and 3 were also important with mode 2 showing considerable sensitivity to changes in stratification. Stacey and Pond (1992), using a numerical model based on hydrographic data sampled in 1983, found net energy fluxes to be about one-half of the Stacey (1985) values. They also showed that both the energy fluxes and energy densities decayed markedly away from the sill. At Tomakstum Island they were about one-half of their value at the generation region. Webb and Pond (1986b) attempted to obtain direct estimates of the distribution of energy flux between the up- and down-inlet M_2 in-

Corresponding author address: Dr. R. F. Marsden, Physics Department, Royal Roads Military College, FMO, Victoria, B.C. V0S 1B0, Canada.

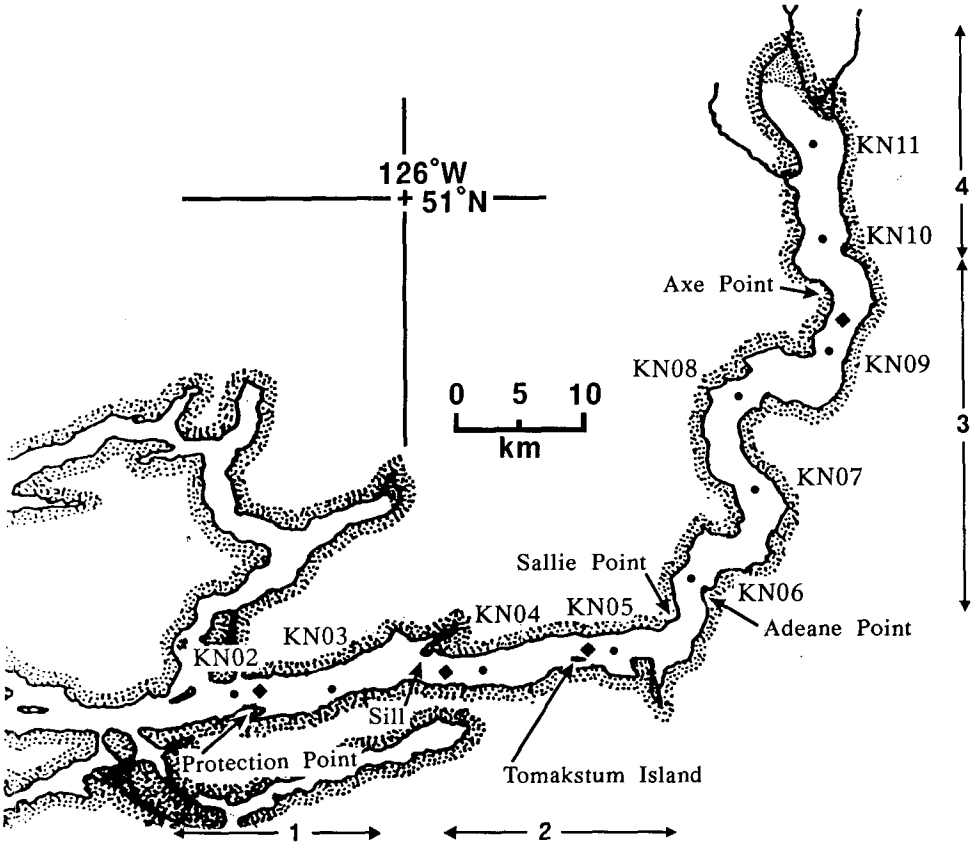

FIG. 1. Chart of Knight Inlet. The dots represent hydrographic stations, the diamonds are the Cyclosonde locations, and the arrows indicate the four geographic regions cited in the text.

ternal tidal wave using an eigenmode decomposition of Cyclesonde records of current and temperature fluctuations. They found that the first and second modes of the vertical eigenvectors of velocity, which formed the basis functions for the least squares solution, were too similar, resulting in a degeneracy in the solution. The indeterminancy resulted in unrealistically large energy flux estimates with net propagation in the wrong direction (i.e., toward the sill). For example, at Tomakstum Island, the energy fluxes were dominated by mode 1 with 8.9×10^6 W directed toward the sill and 8.0×10^6 W directed away from the sill. At this location, they arrived at reasonable energy flux estimates only through arbitrarily eliminating the sillward propagating wave. Farmer and Freeland (1983), in an analysis of four current meter records near Tomakstum Island, concluded that 93% of the amplitude of the internal tide was reflected at Sallie Point east of Tomakstum Island, resulting mostly in a standing internal wave. They avoided the indeterminancy problem by assuming that all the energy was contained in the first dynamic mode. Based on work by Blackford (1984), Freeland (1984) recalculated the problem assuming that all the energy was contained in the second internal mode. He arrived at a revised estimate of 70% reflection. While Webb and Pond (1986b) arbitrarily constrained the reflection coefficient, and Freeland (1984) constrained the energy distribution among the dynamic modes, to date, there has been no totally objective estimate of the strength and distribution of the M_2 internal tide in Knight Inlet.

During June and July 1989, a vessel-mounted acoustic Doppler current profiler (ADCP) study in conjunction with a conductivity–temperature–depth (CTD) study of Knight Inlet was undertaken by Royal Roads Military College (RRMC). An initial assessment of the data can be found in Greenwood (1991). A major finding was that, even though the vessel sampled the inlet at irregular times and places, the baroclinic flow was sufficiently coherent during the month long sampling period to resolve an internal tide signal in the alongchannel velocities. When analyzing data at a single location, the first and second dynamic modes were, as in Webb and Pond (1986), too similar, resulting in degenerate solutions. However, a unique feature of the ADCP is that velocity samples can be made in both time and space. The horizontal phase speeds of the first and second modes were approximately 1.0 m s^{-1} and 0.67 m s^{-1}, respectively. Consequently, the possibility existed that the information inherent in the

data along a cruise track could be exploited to supplement the single station results and hence permit discrimination between modes. This application forms the basis of the present paper. We will show that, when the inlet is broken into regular sections, the ADCP velocity estimates provide unambiguous estimates of both the internal M_2 energy densities and energy fluxes along the inlet. The paper will be organized in the following manner. In section 2 a brief description of the theoretical modal decomposition of the inlet, as used in this study, will be presented. In section 3 the data collection and processing will be described. In section 4 a bulk correlation coefficient between the tidal forcing at the inner sill and the data will be calculated. This will establish optimum correlation and hence signal to noise levels that can be expected in the data. In section 5 a simple WKB model of sections of the inlet will be used to exploit the phase information inherent in the alongtrack velocities to produce unambiguous estimates of the energy fluxes. Finally, section 6 will include a discussion and conclusions.

2. Theory

The phase of a plane wave in a channel may be modified by variations in both channel width and depth. To exploit the horizontal phase information, we require an accurate representation of the phase of the wave as a function of the alongchannel coordinate. We will consider the flow in the inlet to be linear, hydrostatic, and Boussinesq, implying that the water velocity is small compared to the phase speed of the waves (valid except in the region of the sill); that the wavelengths are much larger than the depth of the inlet (always valid for tidal frequencies); and that density variations are important for the vertical but not the horizontal momentum balance. The flow can be considered irrotational if the internal Rossby radius of deformation is much larger than the channel width. This assumption will be made in order to integrate across-channel to determine the effects of variations in channel width on the phase of the wave. The effect of the integration on the alongchannel phase of the internal wave will be shown to be important for modes 1 and 2 and negligible for higher modes. Under these assumptions, equations of conservation of momentum, continuity, and conservation of mass are

$$u_t = -\frac{1}{\rho_\star} p_x, \tag{1}$$

$$p_z = -\rho g, \tag{2}$$

$$u_x + v_y + w_z = 0, \tag{3}$$

$$\rho_t = \frac{\rho_\star}{g} N^2 w, \tag{4}$$

where (x, y) and (u, v) are the (along-, across-) inlet coordinate and velocities, respectively, while z and w are the vertical coordinate and velocity, p is the pressure perturbation, ρ is a density perturbation, $\rho_\star$ is a representative density, and N^2 is the Brunt–Väisälä frequency squared. The positive x axis will be up inlet (or directed toward the head of the inlet) with the origin at KN02 (see Fig. 1), while the z axis will be positive upward with the origin at the mean surface level. If the rays at the bottom reflect about the vertical and if the length scale over which the depth varies is greater than the wavelength, then we can assume a locally flat bottom. Webb and Pond (1986b) provide justification for both criteria being met in Knight Inlet. Consequently, we will assume that the channel width is a function of alonginlet coordinate (x) only. Equation (3) can then be integrated across-channel to give

$$\frac{(uS(x))_x}{S(x)} = -w_z, \tag{5}$$

where $S(x)$ is the channel width. These equations can then be solved to arrive at a governing equation in terms of w:

$$w_{zztt} + \frac{S_x}{S} N^2 w_x + N^2 w_{xx} = 0. \tag{6}$$

Assuming separable solutions of the form

$$w(x, z, t) = \phi(z)\psi(x)e^{-i\omega t}, \tag{7}$$

Eq. (6) separates into

$$\phi_{zz} + \frac{k^2}{\omega^2} N^2 \phi = 0 \tag{8a}$$

and

$$\psi_{xx} + \frac{S_x}{S}\psi_x + k^2\psi = 0, \tag{8b}$$

where k is a separation constant corresponding to the horizontal wavenumber for the constant width channel. Invoking the rigid-lid approximation, appropriate boundary conditions are $w = 0$ at $z = 0$ and $z = -H$. Equation (8a) then takes the form of a Sturm–Liouville problem and numerical solutions can be readily obtained for the vertical eigenvalues (k_n) and eigenvectors (ϕ_n). The eigenvectors were calculated and normalized so that

$$\int_{-H}^{0} \frac{N^2}{\omega^2} \phi_m \phi_n dz = \delta_{mn}. \tag{9}$$

To arrive at the equation for the horizontal velocity we note that Eqs. (1), (2), and (3) can be combined to read

$$u_{ztt} = N^2 w_x. \tag{10}$$

Assuming that

$$u = \sum_{n=0}^{n=\infty} U_n(x) P_n(z) e^{-i\omega t} \tag{11}$$

and substitution of the assumed forms [Eqs. (11) and (7)] into Eq. (5) gives

$$\frac{(U_n S)_x}{S} = -k_n \psi_n, \tag{12}$$

$$P_n(z) = \frac{1}{k_n}\phi_{nz}. \tag{13}$$

Substitution of the assumed forms into Eq. (10) and use of Eqs. (13) and (8a) gives

$$U_n = \frac{\psi_{nx}}{k_n}. \tag{14}$$

Finally, cross-differentiation of Eq. (12) and (14) gives the governing equation for the horizontal dependence of the alonginlet velocity, $U_n(x)$:

$$U_{nxx} + \frac{S_x}{S}U_{nx} + \left[k_n^2 + \left(\frac{S_x}{S}\right)_x\right]U_n = 0. \tag{15}$$

By making the substitution: $U_n(x) = S^{-1/2}\zeta_n(x)$, Eq. (15) becomes

$$\zeta_{xx} + \left[k_n^2 + \frac{1}{2}\frac{S_{xx}}{S} - \frac{3}{4}\left(\frac{S_x}{S}\right)^2\right]\zeta = \zeta_{xx} + \gamma_n(x)^2\zeta = 0, \tag{16}$$

where

$$\gamma_n(x)^2 = k_n^2 + \frac{1}{2}\frac{S_{xx}}{S} - \frac{3}{4}\left(\frac{S_x}{S}\right)^2.$$

This is similar to a one-dimensional wave equation and it is dispersive (or wavelike) for $\gamma_n(x)^2 > 0$ and dissipative (or decaying) for $\gamma_n(x)^2 < 0$. Gill (1982) states that if $d^2\zeta/dx^2$ is small then the WKB approximation may be invoked with approximate solutions given by

$$\zeta = \begin{cases} \gamma_n^{-1/2} e^{\pm i\int_{x_0}^{x}\gamma_n(t)dt}, & \gamma_n^2 > 0 \quad (17a) \\ (-\gamma_n^2)^{-1/4} e^{\pm\int_{x_0}^{x}\sqrt{-\gamma_n(t)^2}dt}, & \gamma_n^2 < 0. \quad (17b) \end{cases}$$

Inclusion of only the phase correction (exponential for $\gamma_n^2 < 0$) is referred to as the geometrical optics solution, while the further inclusion of the amplitude correction is referred to as the physical optics solution. Should γ_n^2 change sign, then approximate matched solutions across the turning point can be found when the wavelength is much less than the horizontal topographic length scale. Bender and Orszag (1978, chapter 10) give a complete discussion of the WKB approximation and the turning point problem.

The vertical density eigenvectors are recovered from Eq. (4):

$$\rho_n(z) = \frac{\rho_\star}{\omega g} N^2(z)\phi(z). \tag{18}$$

Gill (1982) gives the mean perturbation energy per unit volume as

$$E = \frac{1}{2}\rho_\star\overline{u^2 + v^2 + w^2} + \frac{g^2\overline{\rho'^2}}{2\rho_\star N^2}. \tag{19}$$

The time-averaged, vertically and laterally (across inlet) integrated energy density E'_n per unit length of channel for mode n is

$$E'_n = a_n^2\frac{SF_n}{4}\int_0^H \rho_\star u_n^2 + \frac{g^2\rho^2}{\rho_\star N^2}\,dz, \tag{20}$$

where a_n^2 is the amplitude of either the up- or down-inlet propagating wave for mode n; u_n and ρ_n are the normalized vertical velocity and density eigenvectors; and

$$F_n = (\sinh(\delta_n))/\delta_n = 1.0 + \frac{\delta^2}{6} + O(\delta^4)$$

for $\delta_n = S/R_n$, where f is the Coriolis parameter and R_n is the internal Rossby radius of deformation of the nth mode and is a correction term that accounts for the increase in energy density due to rotation. It is 1.00 for mode 1 and about 1.05 for mode 3. Although the theory is cast in terms of irrotational flow, we wish to include a first-order correction for the higher-mode energy densities to ensure that we have not overlooked a possible source of error. The energy fluxes are obtained by multiplying the up-inlet and down-inlet energy densities by the local horizontal group velocities.

3. Data collection and processing

The experiment was conducted from 18 June to 20 July 1989. It consisted of hydrographic and ADCP current meter surveys performed by RRMC personnel and a moored current meter study undertaken by researchers from the University of British Columbia (UBC). For purposes of this study, the inlet was divided into four main regions as shown in Fig. 1. Region 1 comprised the region seaward of the inner sill to Protection Point. Region 2 consisted of the portion up inlet of the inner sill to Sallie Point, while Region 3 extended from Sallie Point to Axe Point and Region 4 extended from Axe Point to the head of the inlet. Of particular importance to this paper are Regions 1 and 2 where the internal tide signal was strongest.

a. Hydrographic survey

The hydrographic data were sampled using a Guildline CTD probe. Eleven hydrographic stations were occupied as shown in Fig. 1. Data within each region were further averaged to create a mean density field for the experiment period. Table 1 indicates the number of casts at, and the region assigned to each station. The CTD was configured to sample only from the surface to 200 m depth. The density data were linearly

TABLE 1. Details of the hydrographic sampling program for the experiment.

Station	Number of casts	Region
KN01	11	1
KN02	11	1
KN03	13	1
KN04	15	2
KN05	16	2
KN06	11	3
KN07	10	3
KN08	11	3
KN09	10	3
KN10	10	4
KN11	10	4

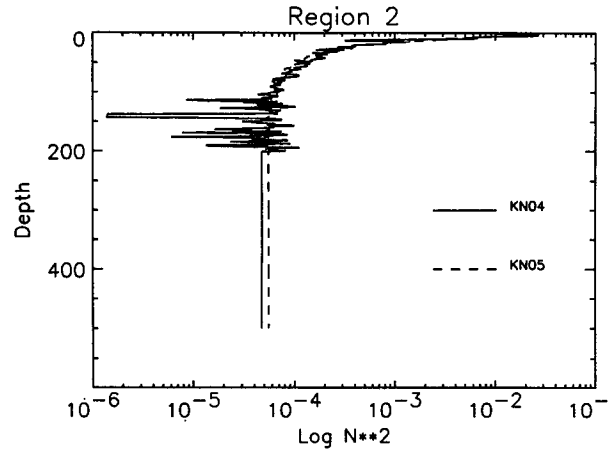

FIG. 2. The Brunt–Väisälä frequencies squared, calculated as a function of depth from the mean density profiles at hydrographic stations KN04 and KN05.

extrapolated to the bottom using the data between 100 and 200 m. This was not a serious assumption because the inlet was highly stratified to only about 50 m depth. The final results were found to be insensitive to alternate extrapolation schemes such as the logarithmic extrapolation of the buoyancy frequency used by Webb (1985). Next, it was assumed that the hydrography was homogenous within regions. Figure 2 shows the Brunt–Väisälä frequency and extrapolation at hydrographic stations KN04, near the sill, and KN05 at Tomakstum Island. Aside from large fluctuations at mid-depth at KN04 caused by turbulence generated at the sill, the mean profiles are nearly identical, indicating that the assumption of regional homogeneity is reasonable. Furthermore, the extrapolated sections extend quite smoothly from the data.

b. *Current data*

The current was sampled by a 150-kHz ADCP manufactured by RD Instruments mounted on the M.V. *Beatrice*. The bin size (vertical resolution) was set to 8 m with a 5-min sampling interval. The electronics were upgraded to include modifications designed to improve performance in regions of high shear (see RDI, 1989 for details). A detailed discussion of the performance of the instrument can be found in Greenwood (1991) and GMB. Only some of the more relevant points will be discussed here. First, the ship heading was corrected using a flux gate compass. Ship position was fixed by a combination of Loran C, and bearing and distance to known points at the hydrographic stations. The intermediate positions were assigned by integrating the bottom track velocity. It was found that mean bottom track directions were systematically 6° clockwise when the vessel was traveling to the east and north (up inlet) and were 6° counterclockwise when traveling to the south and west (down inlet) probably due to local magnetic effects within the vessel. All velocity estimates were corrected for this effect. After correction, the integrated bottom track positions between stations closed to the known locations to within 200 m. To facilitate calculations at single locations, the data were assigned to one of 119 velocity grid points, each with a typical spacing of about 1 km, corresponding to the numerical model grid of Stacey and Pond (1992). The vessel typically traveled at 2.5 m s^{-1} and thus covered three-quarters of a grid point in one 5-minute sampling period. We found that abrupt changes in ship velocity led to erroneous profiles. Consequently, periods of acceleration, deceleration, and rapid change in heading were identified and these records were removed leaving a total of 1526 profiles assigned to grid sites. Figure 3 shows the distribution of sampling along the inlet and the assignment of grid sites to each region. Regions 1 and 2 were selected to avoid sectors of large depth variations and to avoid the area near the sill where the internal tide was expected to be a forced

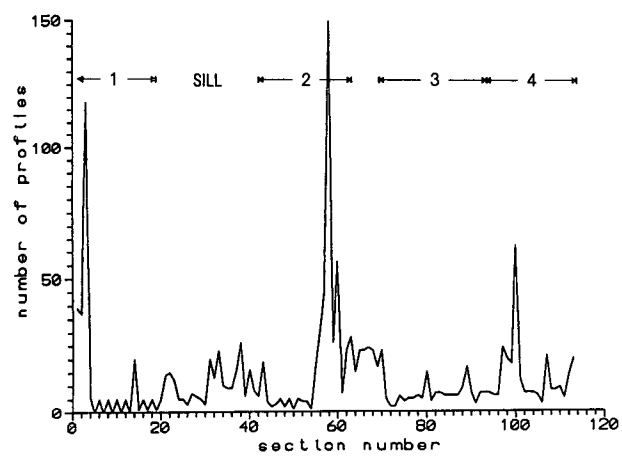

FIG. 3. Distribution of ADCP profiles used in the present study. The inset numbers refer to the regions to which the grid sites were assigned for the study.

rather than a free wave. The large number of profiles at sites 3, 58, and 100 correspond to Protection Point, Tomakstum Island, and Axe Point, respectively, where the Cyclesonde intercomparison was performed. The data were then interpolated by a cubic spline into 8.0-m bins starting at 21.0 m to correspond to the simultaneous Cyclesonde measurements made in the region by UBC, thus allowing for an intercomparison between the two instruments as reported in GMB. A 13.0-m bin was available, but its data were rejected due to a large error induced from signal interference from transducer "ring down" or interference between the transients of the outgoing pulse and the incoming pulse from the first depth bin. Only ensembles with bottom track velocities were accepted. Readings from the bottom 25% of the depth profile were rejected due to side lobe interference. The currents were then resolved into local alongchannel and systematic across-channel components. The overall rms instrument error was estimated in GMB to be 3.9 cm s^{-1}. A barotropic velocity was calculated by taking a vertical average of each 5-min ensemble. A comparison with a simple barotropic tidal prism model yielded a mean rms difference error of 4.2 cm s^{-1} indicating that the depth-averaged velocities were a reasonable estimate of the barotropic component of the alonginlet flow. Finally, the depth-averaged velocities were subtracted from the total velocities to yield 5-min ensemble estimates of the baroclinic velocity profile.

4. Bulk analysis

a. Mean baroclinic residual circulation

There are several examples of the mean baroclinic velocity profile of Knight Inlet in the literature. Pickard and Rodgers (1959) averaged velocity profiles over a 25-h period at the sill and near Tomakstum Island. Webb and Pond (1986b) averaged Cyclesonde velocity profiles over 29 days. The results have shown that a steady circulation cannot be simply defined; that is, there is a great deal of spatial and temporal variation. At Protection Point and Adeane Point, Webb and Pond found mean velocities with the expected outflow at the surface and inflow at depth, although the zero crossings were much deeper than the pycnoline. In contrast, at Tomakstum Island they observed a three-layer flow with inflow at the intermediate depth. Interestingly, the Pickard and Rodgers profiles also show evidence of a three-layer flow near Tomakstum Island, but with *outflow* in the middle layer.

The mean baroclinic velocities for the present study were calculated by an average of the available velocities at four locations, where the distribution of ADCP data was sufficiently dense, and are displayed in Figs. 4a–d. At Protection Point (Fig. 4a), where 118 profiles were averaged together, the alongchannel component shows outflow at the surface and inflow at depth, with a zero crossing at 75 m. This is similar to that found by Webb and Pond (1986b). The cross-channel mean velocity was near zero throughout the water column. At the sill (Fig. 4b), profiles were grouped from 500 m on either side of the crest to increase the number to 76. As a result of the variable depth across the sill, the deeper bins of the profile contribute less to the average. The alongchannel component again shows a two-layer flow, with a zero crossing near 35 m. Considering the highly variable internal flow field that occurs there, the smooth variation in the mean with depth is surprising. The mean residual flow at Tomakstum Island (Fig. 4c) was calculated using 149 profiles. A two-layer flow is still evident with a zero crossing at 120 m. The mean profile of Fig. 4d was the average of 136 profiles sampled within 1 km of KN09, 22 km from the head of inlet. A comparison with the profile standard deviations (not shown) indicates that between 11 and 300 m the mean residual velocities are within noise limits of zero. Evidently the outflow here is confined to the sharply defined surface layer. Below 300 m, the mean is inaccurate due to insufficient sampling. In general, the mean profiles reflect the typical estuarine outflow at the surface and inflow at depth that is expected in an inlet. The mean alongchannel velocities of about 5.0 cm s^{-1} are in agreement with values typically reported. There is no indication, however, of a three-layer structure as reported by Pickard and Rodgers (1959) and Webb and Pond (1986). The discrepancy between the observations suggests that the flow can have inherent variability longer than the 30-day periods used to average the data.

b. Tidal correlations

The spatial and temporal distribution of the ADCP data posed some problems in performing further analyses at a single point in the inlet. For example, at Tomakstum Island, 149 profiles were gathered during the month of the experiment, but were distributed randomly over that time period. Figure 5 shows the sampled residual velocity at 19 m depth as a function of time at Tomakstum Island. Many of the samples appear to be simultaneous. This is an artifact of the long time scale of the abscissa and the relatively short 5-min sampling interval. Despite the obvious discontinuities in the time series, a visual inspection of other residual profiles revealed a consistent variation with depth (not shown) that indicated that the internal signal, although sparsely sampled, was very strong. In almost every residual profile, an outflow near the surface was accompanied by an inflow at depth, and vice versa. This behavior is clearly indicative of internal motion, suggesting that a more comprehensive inspection of the tidal component would be appropriate.

To test this hypothesis, correlations were calculated between the baroclinic alongchannel velocities at Tomakstum Island and the time derivative of the sea surface ($\partial\eta/\partial t$) at the sill for lags up to 24 h in 10-min

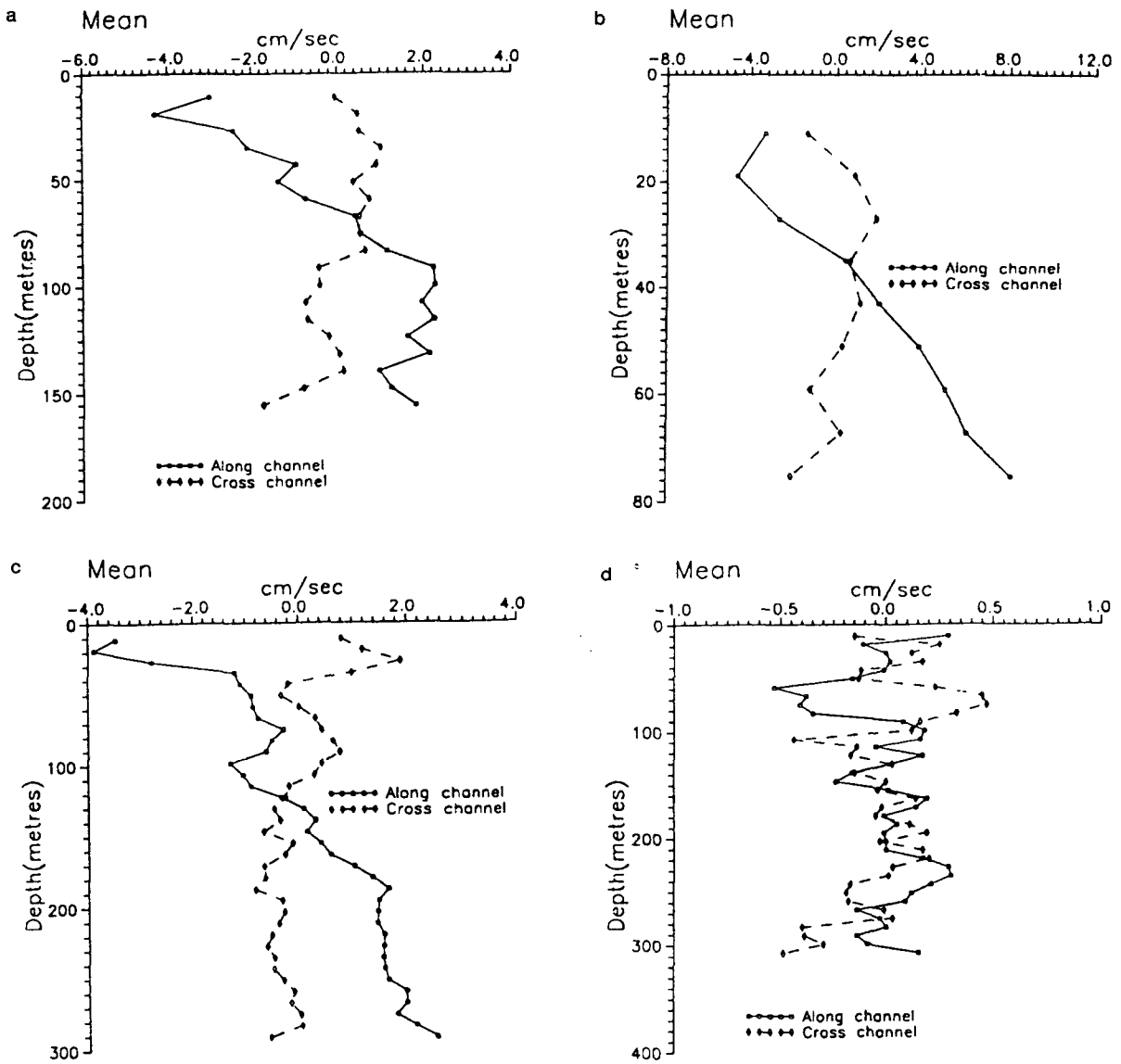

FIG. 4. Mean baroclinic velocity profiles at (a) Protection Point, (b) the sill, (c) Tomakstum Island, and (d) KN09.

increments. Since the barotropic tide can be considered to be a pure standing wave in Knight Inlet, $\partial\eta/\partial t$ is in phase with the barotropic component of the along-channel velocity at the sill. If one assumes that the internal tide is in phase with the surface tide at the generation region (the sill) then the lag correlation provides insight into bulk phase propagation down inlet and the strength of the signal. The lagged correlations were calculated according to the expression:

$$\rho(z, \tau) = \frac{\frac{1}{N}\sum_{j=1}^{N} \hat{u}_i(x, z, t_j)\frac{\partial \eta}{\partial t}(t_j - \tau)}{\sigma_{u_i}\sigma_{\partial\eta/\partial t}}, \quad (21)$$

where N is the number of profiles sampled at a particular location, τ is the lag interval, $\hat{u}_i$ is the residual velocity after the mean baroclinic residual was removed, and $\partial\eta/\partial t$ was obtained from the known tidal height constituents at the sill. Here σ is the sample standard deviation given by

$$\sigma_x = \frac{1}{N-1}\sum_{j=1}^{N}(x_j - \bar{x})^2.$$

The amplitude of the input surface displacement of the M_2 constituent, at the sill, was three times larger than either the S_2 or the K_1 constituents. Since the barotropic velocity is proportional to the frequency times the displacement, assuming that the internal tide generation is roughly proportional to the amplitude of the surface tide, we expect the M_2 constituent to be approximately

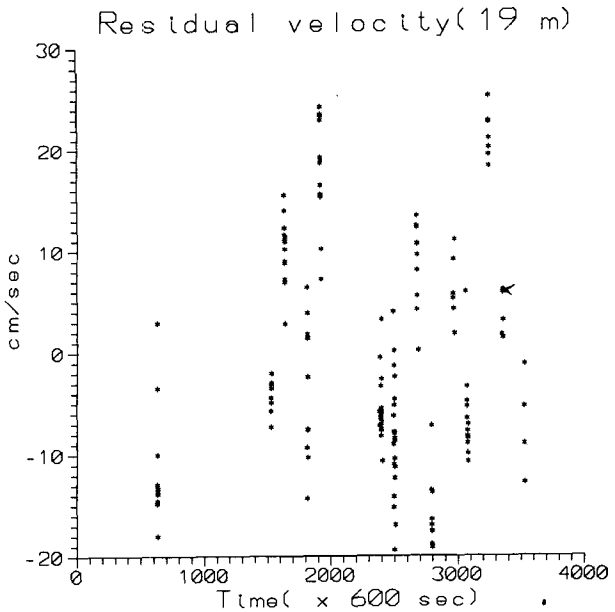

FIG. 5. Distribution of ADCP samples at 19 m depth at Tomakstum Island as a function of time relative to 0000 UTC 24 June 1989.

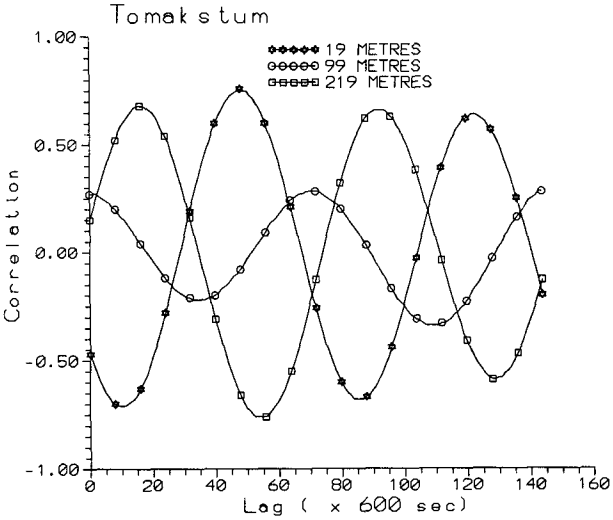

FIG. 6. Lagged correlation coefficients between the tidal forcing $\partial\eta/\partial t$ at the sill and the alongchannel baroclinic velocities at Tomakstum Island at 19, 99, and 219 m depth.

nine times more energetic than the S_2 and 36 times more energetic than the K_1 constitutent.

The calculated lag correlations for three depths at Tomakstum Island are shown in Fig. 6. The results indicate the presence of a strong semidiurnal signal in the residual profiles. Perhaps the most convincing evidence that this is indeed an internal tide is the approximately 180° phase shift in the correlation between the 19 and the 219 m depth. The lag of maximum correlation of 0.85 at the 19-m isobath is 8.0 h. If one assumes that all the energy propagates away from the sill with a uniform phase speed with no reflections at Sallie Point, the time lag corresponds to a phase speed of 43.0 cm s^{-1}. The maximum correlation establishes the noise level of the signal and suggests that a linear regression at the tidal frequencies can account for a maximum of 0.85^2 or 72% of the variability of the alongchannel velocity at Tomakstum at 19 m depth. Figure 7 shows the correlation between the alongchannel velocity at Tomakstum and the six-component tidal signal at the sill as a function of depth for the 8.0-h lag that produced the maximum correlation at 19 m. The curve indicates a zero crossing at 100 m depth. Furthermore, there is a strong negative correlation that peaks at 200 m depth. Next, a linear least squares fit to the M_2 tidal frequency was calculated. The model used was

$$\hat{u}(z, t) = a_0(z) + A(z)\cos(\omega t - \phi(z)), \quad (22)$$

where $a_0(z)$ is a mean term, and $A(z)$ and $\phi(z)$ are the amplitude and phase of the alongchannel velocity as a function of depth. The results are shown in Figs. 8a and 8b along with estimates of the residual error of the fit and error estimates of the parameters. The residual error of about 3.5 cm s^{-1} is very similar to the 3.9 cm s^{-1} reported by GMB. Although the phase used for the M_2 signal was arbitrary, the variation with depth agrees very well with previous estimates by Stacey and Pond (1992) even though the data were sampled during two different time periods.

Similar results were also found at the three other locations with variations in the maximum correlations and hence the signal to noise ratios. At Protection Point, the maximum correlation with the sill tidal signal was 0.6; at KN04 (near the sill), the maximum correlation was 0.6; and at Adeane Point (KN06) the maximum correlation was 0.2 indicating that the signal to noise ratio was markedly reduced around the bend. Finally, the "uniform" phase speed estimates for the stations toward the head of the inlet in relation to the sill are remarkably consistent with a phase speed of

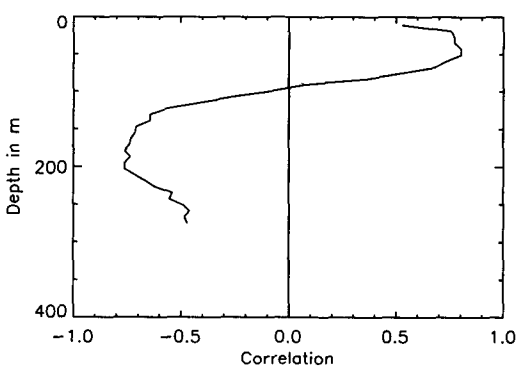

FIG. 7. Correlation coefficient between the tidal forcing $\partial\eta/\partial t$ at the sill and the alongchannel velocity as a function of depth at Tomakstum Island at a lag of 8.0 h.

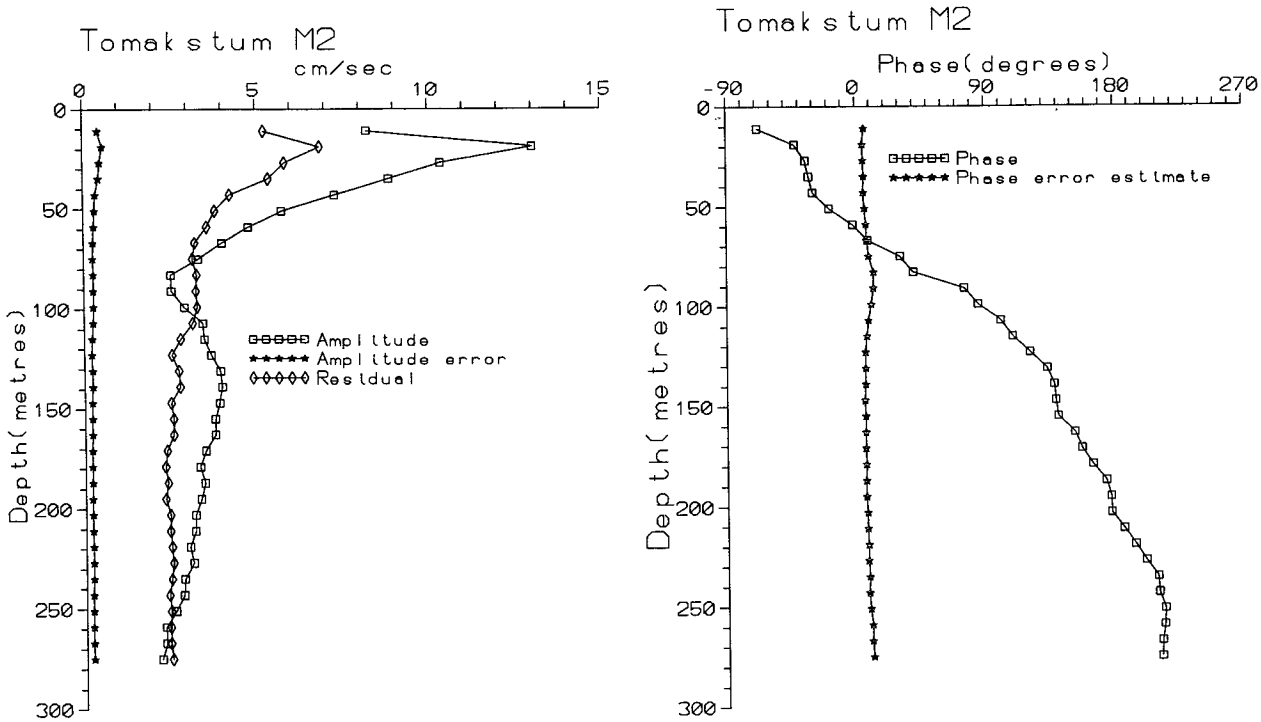

FIG. 8. (a) Amplitude and (b) phase for a harmonic fit of the M_2 tidal frequency to the baroclinic velocities as a function of depth at Tomakstum Island.

37.0 cm s^{-1} at KN04 and a phase speed of 43.0 cm s^{-1} at KN06.

5. Mode fit

The first five dynamic modes were calculated for each velocity site in regions 1 and 2 based on the regional density distribution and the local inlet depth. Next, the baroclinic mean up-inlet velocity was subtracted from the record to produce a baroclinic velocity fluctuation that was fit in a least squares sense to an M_2 tidal model as follows:

$$u(x_i, z_i, t_i) = \sum_{n=1}^{n=5} W^n(x_i)[c_n^+ \cos(\omega t_i - \beta_n(x_i) - \alpha_n^+) + c_n^- \cos(\omega t_i + \beta_n(x_i) - \alpha_n^-)P_n(x_i, z_i), \quad (23)$$

where the summation is over the first five dynamic modes; (c_n^+, c_n^-) and (α_n^+, α_n^-) are the amplitudes and phases for the up- and down-inlet propagating waves, respectively; $W^n(x_i)$ is a horizontal weighting function to be described presently; $P_n(x_i, z_i)$ is the eigenvalue at position x_i and depth z_i; $\beta_n(x_i) = \int_{x_0}^{x} \gamma_n(t)dt$ is the phase function found from the WKB approximation, and ω is the M_2 tidal frequency [0.0805 cycles per hour (cph)]. The phase constants (α^+ and α^-) are arbitrary and depend on the coordinate origin, in our case the coordinate of the first grid point chosen in each region. The fit was performed by recasting the least squares problem in the form

$$\mathbf{u} = \mathbf{Xc}, \quad (24)$$

where $\mathbf{u}$ is the vector of all sampled alonginlet velocities at all depths, site locations, and times within either region 1 or 2; $\mathbf{X}$ is a coupling matrix based on the eigenvectors, times, and phases at each location; and $\mathbf{c}$ are the 20 unknown M_2 tidal coefficients. The matrix inversion was performed by singular value decomposition to monitor any degeneracy inherent in the analysis.

It was found that the fit was sensitive to the assumed widths of the basin, taken to be those corresponding to the grid sites of the Stacey and Pond (1992) numerical model. They were inherently undersampled, resulting in unrealistically large derivatives. Consequently, some smoothing of $S(x)$ (the channel width) was performed as follows. First, the 119 widths were interpolated by a cubic spline from 119 irregular to equally spaced locations. They were then Fourier transformed and the largest 59 minus N independent wavenumbers were set to zero and then inverse transformed. Thus, N refers to the number of independent wavenumbers kept in the inverse transform. This effectively low-pass filtered the set of basin widths. Figure 9 shows a superposition of the raw and low-pass filtered widths for $N = 8$ (Fig. 9a) and $N = 15$ (Fig. 9b); $N = 0$ corresponds to the basin being modeled as a con-

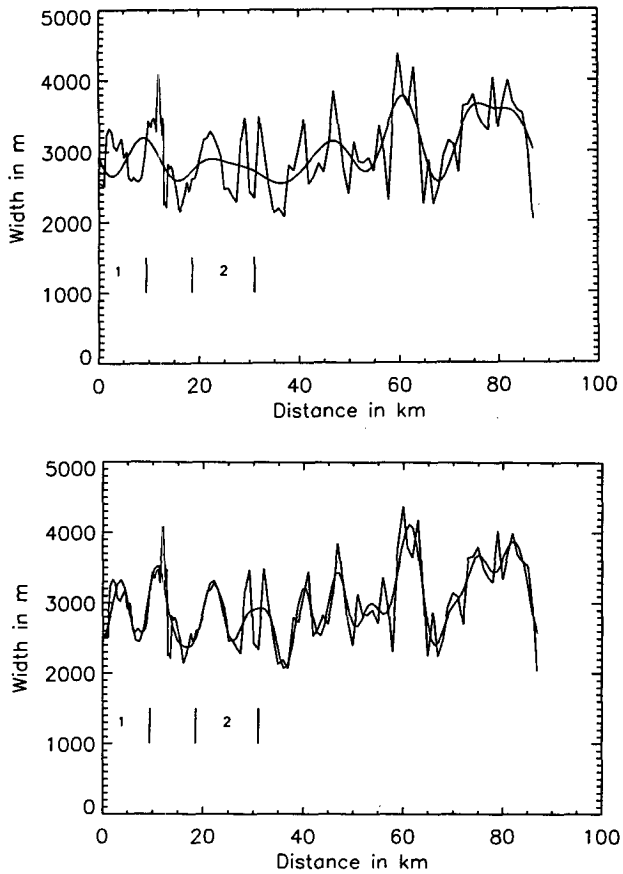

FIG. 9. Comparison between the model and low-pass filtered basin widths for (a) $N = 8$ and (b) $N = 15$, the lowest nonzero wavenumbers of the Fourier transformed basin widths. The inset numbers refer to regions 1 and 2 discussed in the text.

stant mean width. For $N = 15$, filtering preserves the large-scale features while avoiding sharp discontinuities in the first derivatives. The derivatives were then calculated by cubic spline interpolation to the smoothed widths. Figure 10 shows the terms comprising γ_n^2 of Eq. (16): $k_1(x)^2$, $\frac{1}{2}S_{xx}/S$, $-\frac{3}{4}(S_x/S)^2$, and γ_n^2 itself, for $N = 15$ filtering and mode 1 in region 2. The dominant term is $\frac{1}{2}S_{xx}/S$ and is smooth, indicating that the low-pass filtering was effective. The γ_n^2 term is highly correlated with $\frac{1}{2}S_{xx}/S$. It is initially positive, decreases up inlet until $x = 20$ km where a turning point occurs and it becomes negative. Up inlet it remains negative until $x = 25.3$ km where it again becomes positive indicating two turning points and a dissipative portion of the region. Figures 11a and 11b show the velocity phase for $N = 8$ and $N = 15$, respectively, for mode 1 in region 2. For $N = 8$, the corrected phases do not vary markedly from the constant width model $k_1(x)^2$, while for $N = 15$, there are striking variations between the two. A similar situation also occurs for mode 1 in region 1 (Protection Point). Finally, Fig. 11c repeats Fig. 11b for mode 3. It shows that $k_3(x)^2$, the constant width phase function, dominates and that channel width variations do not significantly affect the alongchannel phases.

A physical optics model was initially attempted to account for the two turning points in modes 1 and 2 by assuming exponential decay along the nominal wave directions where $\gamma_n^2 < 0.0$. The approach was abandoned because it led to systematically larger residual errors than for the geometrical optics case and to net energy fluxes propagating toward the sill. This probably occurs because the width length scale is of the same order of magnitude as the mode 1 wavelength, resulting in both significant reflection and transmission at the turning points. Furthermore, the Stacey and Pond (1992) model indicates that sidewall friction and dissipation are important, not taken into consideration in the present model. As a geometrical optics model produced reasonable results, no attempt was made to correct for amplitude variations along the inlet with the phase difference across the dissipative portions assumed to be zero (reflected in the flat segment of the curve of Fig. 11b). Consequently, $W(x_i)$ in Eq. (22) was set to $S(x_i)^{-1/2}$ to account for the transformation of Eq. (16). The energy densities and fluxes were calculated at Protection Point in region 1, and Tomakstum Island in region 2, where the majority of measurements were made. Thus, the fit was heavily weighted at these two sites while the measurements along the cruise track were used to resolve the degeneracy in undersampling the surface layer and to discriminate between the up- and down-inlet propagating waves.

The fit was tested for sensitivity to changes in estimated width variations. For the two sites, the effect of increasing the number of nonzero wavelengths (N) of the inverse transform was determined. Table 2 shows the residual error, energy densities, and energy fluxes

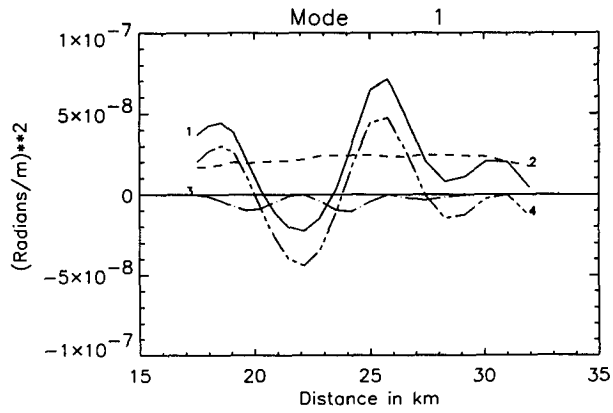

FIG. 10. Plot of the terms composing Eq. (16) for mode 1, region 2, and the lowest $N = 15$ nonzero width wavenumbers. The inset numbers correspond to 1) γ_n^2 the apparent wavenumber squared, 2) $k_1(x)^2$ the wavenumber squared for the uniform width model, 3) $-\frac{3}{4}(S_x/S)^2$, and 4) $\frac{1}{2}S_{xx}/S$. The origin is relative to KN02.

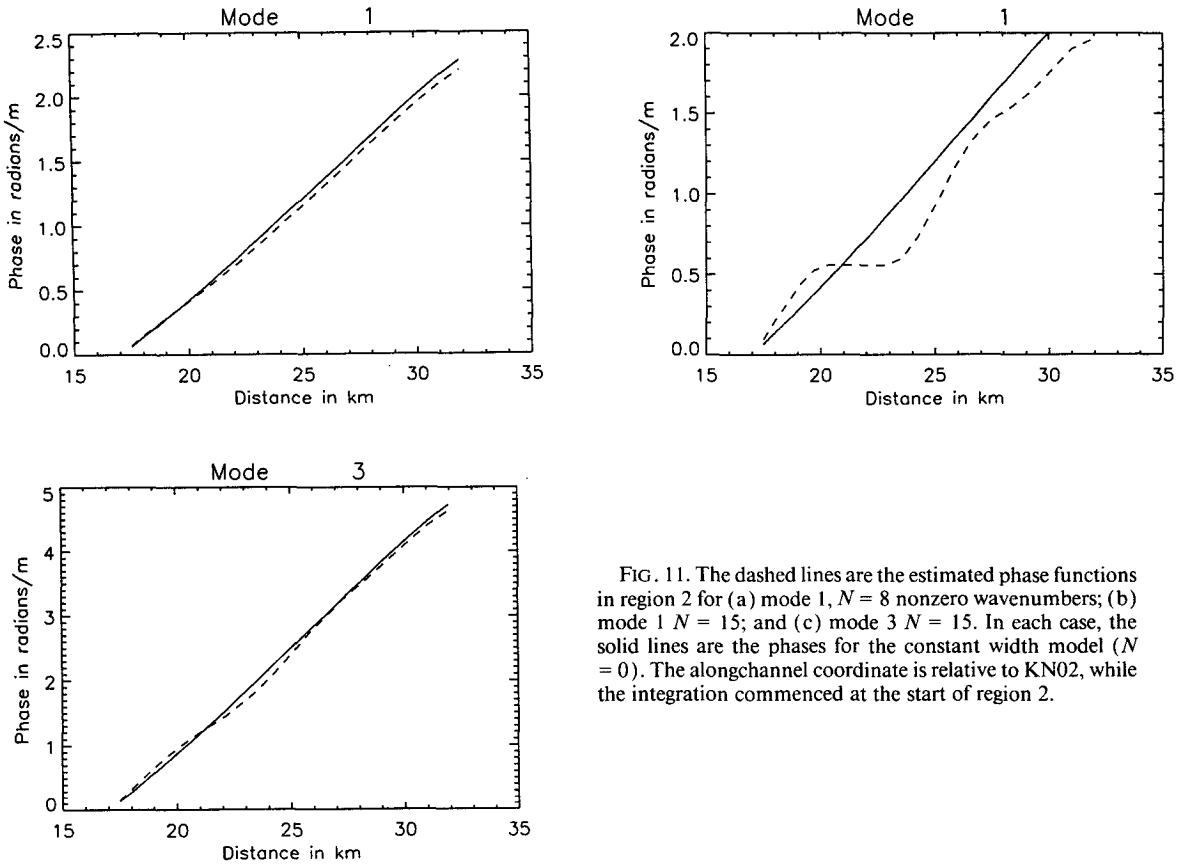

FIG. 11. The dashed lines are the estimated phase functions in region 2 for (a) mode 1, $N = 8$ nonzero wavenumbers; (b) mode 1 $N = 15$; and (c) mode 3 $N = 15$. In each case, the solid lines are the phases for the constant width model ($N = 0$). The alongchannel coordinate is relative to KN02, while the integration commenced at the start of region 2.

calculated for the two regions for $N = 0$ (no width variations) and $N = 8$–18. The residual error is about 75.3% at Protection Point and 55.3% at Tomakstum Island. In both cases it is insensitive to changes in estimated width variations. This occurs because the data in each region are dominated by a single grid point. Consequently large variations in the fit along the track contribute little to the overall residual variance. At Protection Point, the energy density is relatively constant with a mean value of 3.5×10^6 J m^{-1}, while the energy flux has a maximum of 1.66×10^6 W down inlet for $N = 8$, which decreases to a relatively constant value of 0.43×10^6 W down inlet by $N = 15$ wavelengths. At Tomakstum both the energy densities and the energy fluxes show considerable variability for $N < 12$ but again relatively constant values of 3.6×10^6 J m^{-1} and 1.17×10^6 W up inlet are achieved by $N = 15$ wavelengths. The transition to the stable energy densities begins at $N = 12$ for both locations, which also corresponds to the width structure where the turning points and dissipative segments first appear.

To demonstrate that the problem is not degenerate, Table 3 contains the energy distribution for $N = 15$ wavelengths of width variations for the two locations. For both locations, mode 1 is dominant. At Tomakstum, small but significant energy fluxes are found for modes two and three. All the other modes show insignificant energy fluxes and densities. The apparent reflection coefficient (the square root of the ratio of the sillward propagating energy flux to outward propagating energy flux) for mode 1 are 0.80 for Protection Point and 0.66 at Tomakstum. At neither location is there evidence of degeneracy in the matrix inversions, as all energy fluxes are either small or reasonably bounded. Furthermore the singular value decomposition showed a ratio between the largest and smallest singular values of 28 at Protection Point and 46 at Tomakstum, clearly indicating stable inversions. A value much greater than 1000 would indicate degenerate solutions. Also shown in Table 3 are the energy calculations from Stacey and Pond (1992). Our results indicate slightly larger energy densities but virtually identical energy fluxes to theirs, indicative of somewhat more reflected energy than calculated in the numerical model. Finally, the rms residual error of 4.5 cm s^{-1} at Protection Point and 3.4 cm s^{-1} are not significantly different from the noise level of 3.9 cm^{-1} for the instrument found by GMB suggesting that an increase in the number of tidal constituents will not improve the fit.

6. Discussion and conclusions

There are two major results from this study. First, by using the alongtrack phase information from the

TABLE 2. Sensitivity of the fit to changes in channel width. Here, N indicates the number of frequencies retained in the low-pass filter. A positive energy flux indicates a net up-inlet (toward the head) energy propagation.

Grid	N	Residual error (%)	Energy density ($\times 10^6$ J m^{-1})	Energy flux ($\times 10^6$ W)
Protection	0	75.38	3.31	−1.64
Point	8	75.31	3.24	−1.66
(Region 1)	9	75.37	3.32	−1.58
	10	75.34	3.43	−1.42
	11	75.28	3.39	−1.36
	12	75.33	3.61	−0.60
	13	75.32	3.62	−0.96
	14	75.36	3.65	−0.44
	15	75.31	3.41	−0.43
	16	75.34	3.48	−0.32
	17	75.36	3.72	−0.47
	18	75.37	3.83	−0.54
Tomakstum	0	55.62	1.58	0.57
Island	8	55.82	1.62	.61
(Region 2)	9	55.69	1.88	.73
	10	55.24	3.03	1.33
	11	55.10	3.55	1.45
	12	55.47	1.81	.84
	13	55.49	1.68	0.92
	14	55.39	2.72	1.08
	15	55.24	3.64	1.17
	16	55.20	3.81	1.18
	17	55.18	3.65	1.03
	18	55.25	3.26	0.97

ADCP, we have obtained estimates of the energy densities and energy fluxes at two locations along Knight Inlet without setting a priori conditions on either the mode structure of the internal tide [as in Farmer and Freeland (1983) and Freeland (1984)] or on the reflection coefficient [as in Webb and Pond (1986b)]. Furthermore, the results do not exhibit the large up- and down-inlet energy fluxes, indicating a singular matrix inversion, which was further confirmed by the small ratio of maximum to minimum singular values found in the singular value decomposition. Net energy fluxes of approximately 1.18×10^6 W away from the sill at Tomakstum and 0.44×10^6 W away from the sill at Protection Point were calculated. These are in close agreement with the values calculated by Stacey and Pond (1992), and with the net flux calculated by Webb and Pond (1986b) at Tomakstum. We found that the flow was dominated by mode 1 at both locations. The reflection coefficient 0.66 found at Tomakstum Island is somewhat less than the 0.90 found for the mode 1–dominated estimate of Farmer and Freeland (1983). It must be emphasized, however, that the results cited are for different sampling years. Deep-water renewal and interannual variability in river runoff can affect the density structure and hence the mode structure of the inlet. Stacey (1985) has shown theoretically that there is considerable variation in the annual and interannual internal tide generation at the sill. Consequently, the agreement shown here may be somewhat fortuitous.

Second, the phase function for modes 1 and 2 were found to depend critically on fluctuations in channel width. Clearly, any calculations involving alongchannel phase, such as propagation calculations between current meter arrays deployed alongchannel must account for this effect. Furthermore, the large apparent reflection coefficients at both locations may be due to channel width variations. Freeland (1984) proposed that the 90° bend in the channel at Sallie Point was responsible. In a theoretical investigation, Webb and Pond (1985) showed that the reflection coefficient for internal Kelvin waves of the scale to be found in Knight Inlet was less than 5% for a right-angled corner and hence not a factor. The shoaling bottom topography between Tomakstum Island and Sallie Point could be a further cause of wave reflection. Variations in bottom topography were not considered in this study. However, the first dynamic mode is highly surface intensive and hence decoupled from the bottom topography. Consequently, one would expect it to be insensitive to this effect. Another possibility is that there are alternate

TABLE 3. Results of the free wave M_2 least squares fit for $N = 15$ wavelengths of topographic variability.

Protection point

Number of available data points 3594
% residual variance 75.3%
Rms residual error 4.5 cm s^{-1}

Mode	Energy density ($\times 10^6$ J m^{-1})	Energy flux ($\times 10^6$ W) Down inlet	Up inlet
1	2.83 ± .30	−1.38 ± .13	+0.87 ± 0.11
2	0.11 ± .04	−0.00 ± .03	+0.06 ± 0.02
3	0.16 ± .04	−0.01 ± .01	+0.04 ± 0.01
4	0.25 ± .08	−0.04 ± .01	+0.03 ± 0.01
5	0.06 ± .05	−0.01 ± .01	+0.01 ± 0.01
Total	3.41 ± .51	−1.45 ± .19	+1.01 ± 0.16
Net		−0.44 ± .35	
Stacey and Pond (1992)	3.0	−0.4	

Tomakstum Island

Number of available data points 10 732
% residual error 55.24%
Rms residual error 3.4 cm s^{-1}

Mode	Energy density ($\times 10^6$ J m^{-1})	Energy flux ($\times 10^6$ W) Down inlet	Up inlet
1	2.16 ± 0.06	−0.61 ± 0.02	+1.37 ± 0.03
2	0.91 ± 0.05	−0.18 ± 0.01	+0.43 ± 0.02
3	0.36 ± 0.02	−0.02 ± 0.01	+0.14 ± 0.01
4	0.11 ± 0.01	0	+0.04 ± 0.005
5	0.11 ± 0.02	−0.01 ± 0.002	+0.02 ± 0.002
Total	3.64 ± 0.16	−0.82 ± 0.04	+2.00 ± 0.07
Net			1.18 ± 0.11
Stacey and Pond (1992)	2.2		1.0

generation sites for the internal tide. If there were other major generation regions one would expect areas of increased energy density. The Stacey and Pond (1992) model, however, shows only uniform decay away from the sill. It is proposed that the variations in channel width are responsible for the apparent large reflections at both locations. We have shown that the propagation of the mode 1 wave was very sensitive to the estimated channel width, while the mode 3 wave was virtually unaffected. The results at Tomakstum Island (Table 3) indicate 66% and 65% reflection, respectively, for modes 1 and 2, while that of mode 3 is only 38%, supporting this proposal.

Acknowledgments. RFM acknowledges the support of the Academic Research Program of the Canadian Department of National Defence. Dr. M. W. Stacey lent us initial results from his numerical model of the inlet and contributed many fruitful discussions on fjord oceanography in general and Knight Inlet in particular. We greatly appreciate Dr. S. Pond's generosity in allowing us to participate in his experiment and for donating some of his Cyclesonde data for the intercomparison study.

REFERENCES

Bender, C. M., and S. A. Orszag, 1978: *Advanced Mathematical Methods for Scientists and Engineers.* McGraw-Hill, 593 pp.

Blackford, B. L., 1984: Effect of a tidal stream on internal wave observation and predictions. *Atmos.-Ocean,* **22,** 125–143.

Farmer, D. M., and H. J. Freeland, 1983: The physical oceanography of fjords. *Progress in Oceanography,* Vol. 12, Pergamon Press, 147–219.

Freeland, H. J., 1984: The partition of internal tidal motions in Knight Inlet, British Columbia. *Atmos.-Ocean,* **22,** 144–150.

——, and D. M. Farmer, 1980: Circulation and energetics of a strongly stratified inlet. *Can. J. Fish. Aquat. Sci.,* **37,** 1398–1410.

Gill, A. E., 1982: *Atmosphere-Ocean Dynamics.* Academic Press, 662 pp.

Greenwood, K. C., 1991: Performance of an Acoustic Doppler Current Profiler in Knight Inlet, British Columbia. M.S. thesis, Physics Department, Royal Roads Military College, Victoria, British Columbia, 99 pp.

——, R. F. Marsden, and J. R. Buckley, 1993: Performance of an Acoustic Doppler Current Profiler in Knight Inlet, British Columbia. *Atmos.-Ocean,* **1,** 297–318.

Pickard, G. L., and G. K. Rogers, 1959: Current measurements in Knight Inlet, British Columbia. *J. Fish. Res. Bd. Can.,* **16,** 635–678.

RDI, 1989: Velocity measurement bias in the ADCP. RD Instruments Technical Bulletin ADCP-89-06, 24 pp.

Stacey, M. W., 1985: Some aspects of the internal tide in Knight Inlet, British Columbia. *J. Phys. Oceanogr.,* **12,** 1652–1661.

——, and S. Pond, 1992: A numerical model of the internal tide in Knight Inlet, British Columbia. *Atmos.-Ocean,* **30,** 383–418.

Stigebrandt, A., 1976: Vertical diffusion driven by internal waves in a sill fjord. *J. Phys. Oceanogr.,* **6,** 486–495.

——, 1979: Observational evidence for vertical diffusion driven by internal wave of tidal origin in the Oslofjord. *J. Phys. Oceanogr.,* **9,** 435–441.

——, 1980: Some aspects of tidal interaction with fjord constrictions. *Estuarine Coastal Mar. Sci.,* **11,** 151–166.

Webb, A. J., 1985: The propagation of the internal tide around a bend in Knight Inlet, B.C. Ph.D. thesis, University of B.C., Vancouver, Canada, 160 pp.

——, and S. Pond, 1986a: The propagation of a Kelvin wave around a bend in a channel. *J. Fluid Mech.,* **169,** 257–274.

——, and ——, 1986b: Modal decomposition of the internal tide in a deep, strongly stratified inlet: Knight Inlet, British Columbia. *J. Geophys. Res.,* **91,** 9721–9738.